


Article

Investigation on Effective Thermal Conductivity of Fibrous Porous Materials as Vacuum Insulation Panels' Core Using Lattice Boltzmann Method

Bangqi Chen ¹, Ankang Kan ^{1,*} , Zhaofeng Chen ², Jiaxiang Zhang ¹ and Lixia Yang ²¹ Merchant Marine College, Shanghai Maritime University, Shanghai 201306, China² College of Material Science and Technology, Nanjing University of Aeronautics and Astronautics, Nanjing 210016, China* Correspondence: ankang0537@126.com

Abstract: Vacuum Insulation Panels (VIPs) provide significant adiabatic performance for heat/cooling systems to reduce energy consumption. The application of fibrous porous material (FPM) as the ideal core of VIPs has gained global attention in recent decades. The microstructure and physical properties of FPMs, filled as novel VIPs' core material, and holding superior thermal performance, affected effective thermal conductivity (ETC) greatly. Aiming to deeply understand heat transfer mechanisms, a holistic simulation method that combined with a developed 3D FPM structure generation method and a D3Q15-Lattice Boltzmann method (LBM) is proposed to simulate the heat transfer in FPM and to illuminate the influence factors of ETC on the microstructure of FPM in a vacuum. The improved and modified mesoscopic 3D fibrous random micro-structure generation approach involved five structural parameters: generation probability of nucleus growth, fiber length, diameter, coincidence rate, and orientation angle. The calculation model of ETC is established, and the discrete velocity, distribution, evolution, and boundary conditions of D3Q15-LBM are invested in detail. The model is validated with influences of different microstructure parameters. It indicated that FPM with finer diameter, smaller average pore size, and bigger orientation angle easily gain the lower ETC in a vacuum. The ETC was also affected by the orientation angles of fibers. The more the heat transfer direction is inconsistent with the length direction of the fiber, the better the adiabatic performance is. The reliability of the model is verified by comparison, and this work is a reference to optimize the fibrous core of VIPs.

Keywords: vacuum insulation panel; fibrous porous materials; effective thermal conductivity; Lattice Boltzmann method; mesoscopic scale



Citation: Chen, B.; Kan, A.; Chen, Z.; Zhang, J.; Yang, L. Investigation on Effective Thermal Conductivity of Fibrous Porous Materials as Vacuum Insulation Panels' Core Using Lattice Boltzmann Method. *Energies* **2023**, *16*, 3692. <https://doi.org/10.3390/en16093692>

Academic Editors: Chi-Ming Lai and Ákos Lakatos

Received: 2 March 2023

Revised: 31 March 2023

Accepted: 24 April 2023

Published: 25 April 2023



Copyright: © 2023 by the authors. Licensee MDPI, Basel, Switzerland. This article is an open access article distributed under the terms and conditions of the Creative Commons Attribution (CC BY) license (<https://creativecommons.org/licenses/by/4.0/>).

1. Introduction

Global climate change, along with carbon emissions, threatens the international community [1]. Focusing on Chinese carbon emissions, the government has announced its aim to reach peak emissions before 2030, and further become carbon neutral before 2060 [2]. Although the Chinese allowance of total carbon emission before 2030 has not yet been officially determined, every effort will be made to reach the peak ahead of time. This has been allocated to different provinces and cities where emission reduction actions are primarily implemented [3]. The Chinese carbon emission peak is estimated to be hit around 2025, five years ahead of 2030, thanks to the effort of energy transformation and conservation [4]. Thermal insulation material is an effective pathway to reduce energy consumption, which is honored as the fifth energy source after coal, petroleum, nuclear energy, and natural gas [5–10]. To achieve the double carbon goals, the innovation and application of super insulation materials in China have become an urgent and active discussion and concern [4–15].

With their thermal superiority, vacuum insulation panels (VIPs) are admired as one of the super adiabatic materials [16]. Its thermal conductivity is always $2\text{--}8\text{ mW}\cdot\text{m}^{-1}\cdot\text{K}^{-1}$, much lower than common insulation materials ($20\text{--}120\text{ mW}\cdot\text{m}^{-1}\cdot\text{K}^{-1}$). A classical VIP mainly consists of a porous core material, a barrier envelope, and a getter, if necessary, As introduced by H. Simmler et al. [17].

Our diagrammatic sketch of a VIP is shown in Figure 1. The porous core is composed of a solid skeleton and inter-connected cells, which are significant in energy exchange and storage [18,19]. They can be applied to insulation systems due to their excellent properties. The primary function of barriers is to prevent moisture and gases from permeating into the core, maintaining internal pressure.

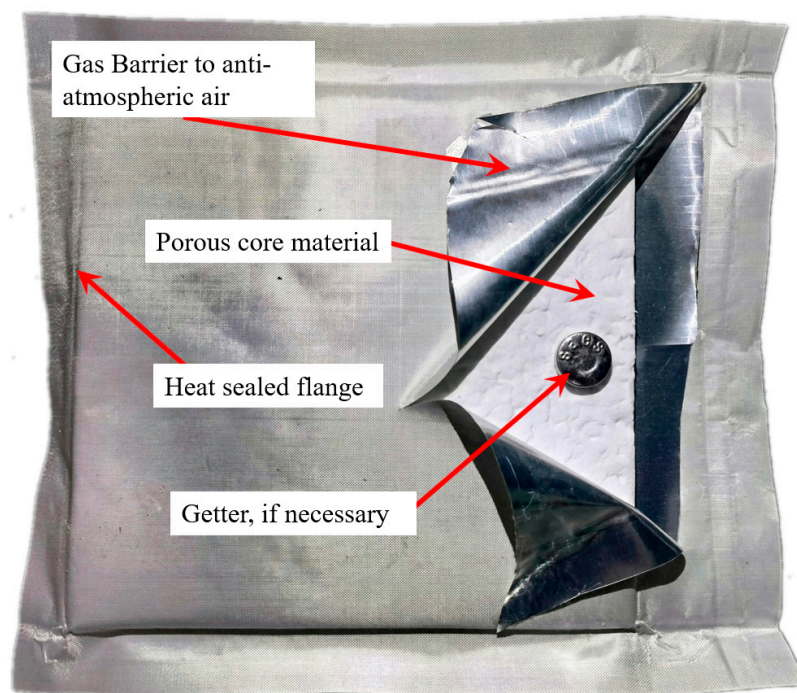


Figure 1. Constitution of VIP (manufactured and photographed by authors' team).

Fibrous porous materials (FPM) were widely used as the core of VIPs. Many simulated and experimental research studies have been performed in the literature of science and technology in the last decade. A general comprehension of the two-phase heat exchange mechanisms inside the core is vital to improve the adiabatic performance of VIP [20]. As we all know, heat transfer in FPM depends on the thermal properties and porosities of all components. However, it is nearly impossible to control or measure microstructures of FPM by the experimental method in a direct way, because of its anomalous characteristics. So, the understanding of the effects of the different parameters on the contributions that make of the heat transfer in FPM required a model with high precision and feasibility. Simulations can indicate the actual pore structure based on macroscopic parameters to illuminate the effect of micro geometric factors on heat transfer in FPM. Two categories were introduced in the notable present literature; one is the idealized elementary units, while the other is steerable stochastic generation.

In the last decade, many novel research studies have predicted the ETC. Wang et al. [21], Alessandro Tugnoli et al. [22], Tian Xiao et al. [23], Wang et al. [24], Mendes et al. [25], and Yixiong Lin et al. [26] proposed microscopic models of random generation and proposed a method to evaluate ETC. Wei et al. [27], Bi et al. [28], and Farahani, M. V. et al. [29] conducted a mechanistic study on pore-scale mechanisms in partially saturated porous media. A numerical model was developed for the prediction of ETC using LBM, and the model was validated with the experimental data to assess its accuracy against the existing models. A D3Q19-BGK was proposed by Lu et al. [16] to research

the ETC in a vacuum. Qu et al. [30] presented a method to simulate heat transfer in FPM based on LBM and generated its porous geometry, but it was only implemented in two dimensions. Jesse et al. [31] established a tool to generate geometry and then automatically simulate the ETC.

In macro continuum models, the material is regarded to be continuous and uninterrupted. The established series of partial differential equations involving macro physical quantities (such as pressure, velocity, density, and temperature) and time were used to describe various macro motions. In micromolecular dynamics models, materials are considered to be composed of a large number of molecules. Every molecule was studied, using Newton's law of motion, to describe the overall flow characteristics based on statistical methods. Due to the limitations of continuity assumptions, the continuum model is no longer applicable to some microscopic problems. The subsequently developed mesoscopic kinetic theory, LBM, is a mesoscopic model that lies between the aforementioned macroscopic continuum model and the microscopic molecular dynamics model. LBM is regarded as the macroscopic motion is the average statistical result of the thermal motion of all molecules.

To evaluate thermal properties in FPM, the temperature distribution in systems [32,33], types of porous materials [34,35], and heat transfer models of porous materials are impotent. However, while all the above generation methods have been widely and highly employed to generate various porous materials, they can hardly be applied to the FPM because of its long strip shape. Therefore, research effort went into this study of its microstructure and thermal properties. In this work, a developed D3Q15-LBM for procedurally generating and simulating heat transfer through FPM is presented. The modified method provided a distinct advantage over other approaches in this paper. The measurement system to measure the ETC of VIPs is also presented. The simulation results are discussed, and suggestions are given to improve the ETC of VIPs.

2. Model and Methods

Microstructural models present ideal geometries constructed from periodic arrays of the regular pore. The consequence of the model is that the stochastic properties of the microstructures are neglected for porous media, and attention is focused only on the effect of the pore shape and ligament nodes on thermal performance. As one kind of common porous material, FPM inherently owns a random microporous network structure with high porosity, and pores are normally intruded by various fluids, such as water and air.

As we all know, DmQn (m is dimension and n is growth direction) model is the basic model of LBM. The D3Q15 is implied in Figure 2.

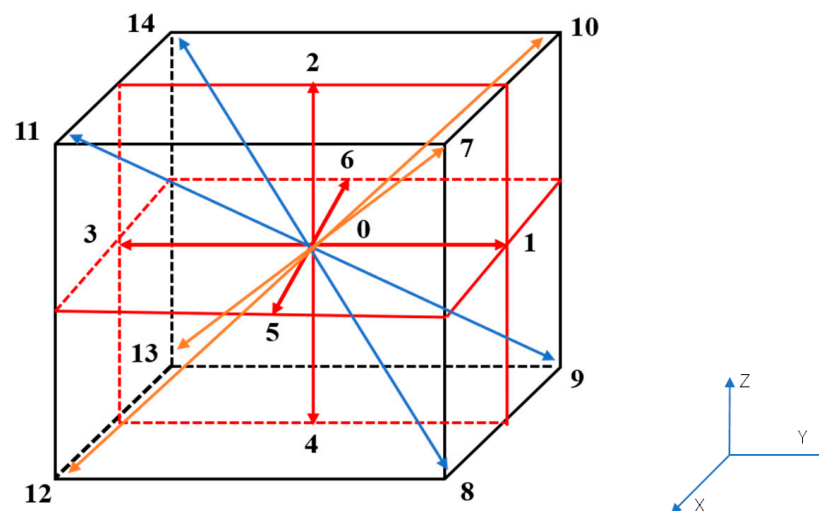


Figure 2. The LBM model of D3Q15: Numbers 0–14 are growth directions.

Two steps were followed. FPM geometry was first generated by D3Q15, and then the ETC of FPM was simulated by CFD. The two steps were followed by the physical measurements of ETC, which were involved to compare with simulated results.

2.1. Geometry Generation Approach

D3Q15-LBM was introduced to simulate the microstructure of FPM. The solid fibers are generated and distributed in random manner, and the connections are also randomly constructed according to the growth of the solid skeleton. The D3Q15 model is utilized for three-dimension calculation. The solid fiber phase is selected as the growth phase, and the gas (invaded pores) is selected as the non-growth phase.

The real Microstructure of FPM was scanned by electronic scanner apparatus. The scanning electron micrographs (SEM) for FPM are shown in Figure 3. The real microstructure parameters can be easily gained by SEM, and the key parameters (such as fiber average diameter, fiber average length, and orientation angle) were collected. All parameters clearly named physical mean to ensure the stochastic properties of the microstructure. From the SEM, we can easily find that the reality microstructure of FPM is random, and the fibers for structural composition are irregular, instead of tetrahedral or hexahedral. Therefore, considering the stochastic properties, the D3Q15-LBM is appropriate to reconstruct the microstructure model, which is closer to the reality microstructure. Microstructure reconstructing process of FPM is illustrated in Figure 4.

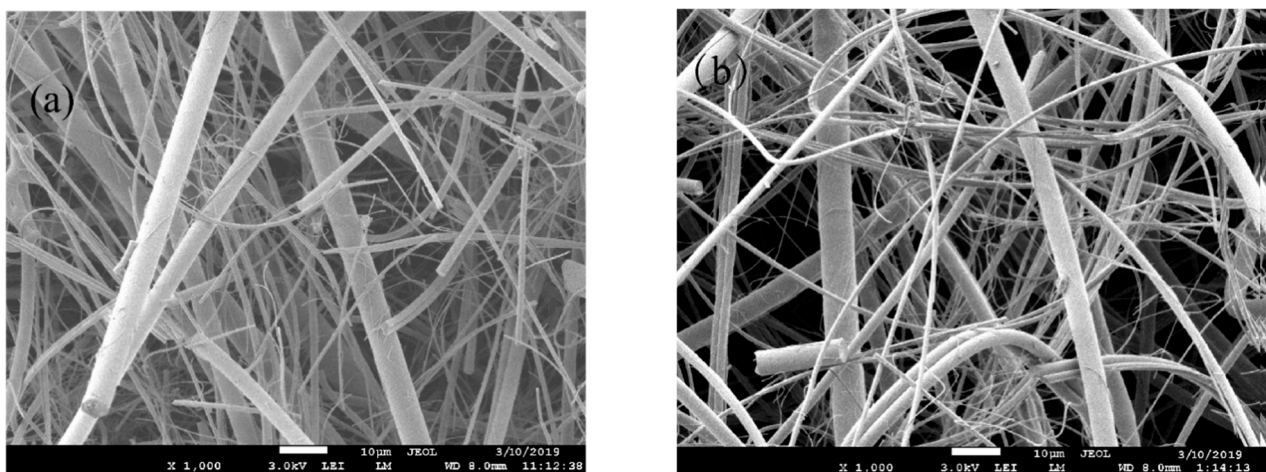


Figure 3. SEM image of FPM and quantities: the average diameter (a,b) was 4.3 μm and 5.4 μm , respectively.

After microstructure of the FPM was obtained in SEM, the images were then imported into our MATLAB program. The preprocessing of image handling includes image clipping, filtering, histogram equalization, gray scale adjustment, linear sharpening, binarization, and so on. After image binarization, the solid-phase volume fraction of FPM can be calculated, and the parameters from SEM can be imported into the D3Q15 LBM program.

Given the fact that the noise reduction is at the expense of image blurring in the filtering proceeding, while the clarity of the SEM is not high, the contrast between the target and the background leads to deviation between the established model and the actual internal structure. Therefore, median filtering method is used for image filtering in this work. Histogram equalization can automatically enhance the contrast of the images, facilitating the binarization proceeding to distinguish between the target and background colors.

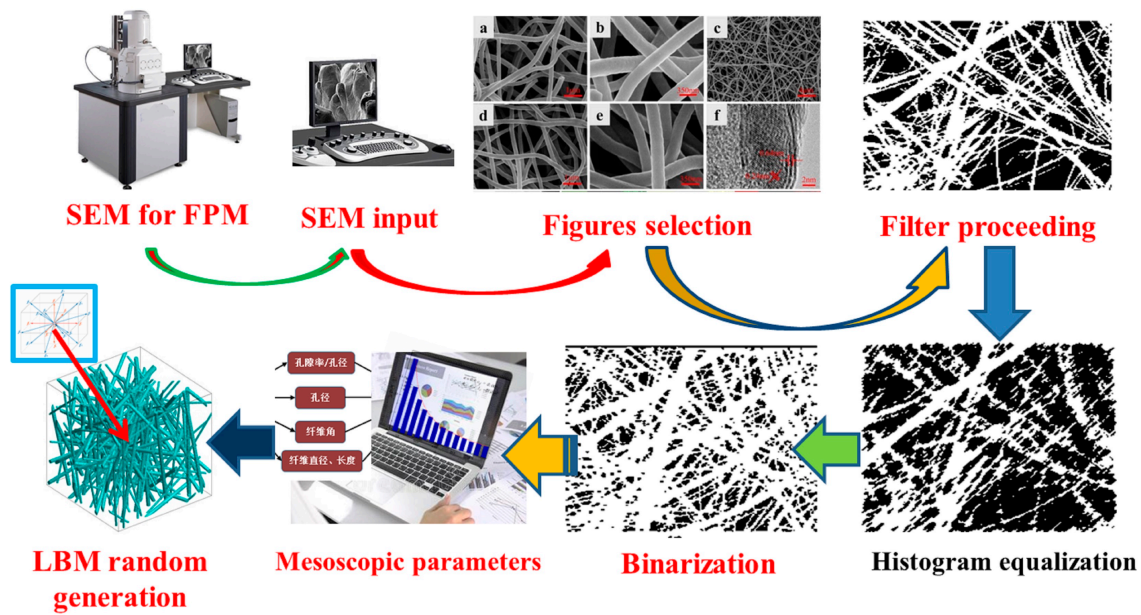


Figure 4. The microstructure generating procedure for FPM: (a–f) are random images with different magnifications. 孔隙率/孔径: porosity/bore diameter; 孔径: bore diameter; 纤维角: fiber angle; 纤维直径/长度: fiber diameter/length.

FPM mainly consists of solid fiber and the fluid that invades the pores (usually air and water). The solid phase is selected as generation phase, and the gas (invaded pores) as non-growth phase. The developed model of FPM is described in Figure 5. The steps are illustrated as follows:

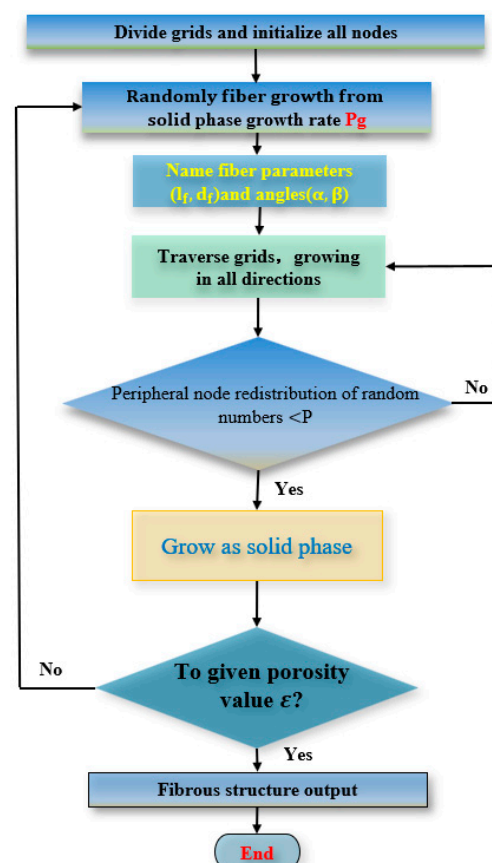


Figure 5. Construction program of D3Q15-LBM.

Generating cube domain is selected, mesh is divided, and all meshing nodes are initialized. All grid nodes ($N_x \times N_y \times N_z$) are initialized to fluid phase. Based on the given solid-phase growth rate P_g (P_g is not greater than solid-phase volume fraction, $1 - \varepsilon$), the solid-phase fibers are randomly distributed on the grid nodes. A non-solid growth core (x_0, y_0, z_0) is randomly located based on a given constant core distribution probability, c_d . Each node in the region is traversed, and a random number is generated within the (0, 1). If the given random number is less than P_g , the node is a solid-phase fiber. Otherwise, the node is not a solid-phase core.

Inclination angle α and azimuth angle β are defined to evaluate the fiber growth direction; α is the angle between fiber and z-axis, β is the projection angle between fiber and y-axis in plane Z, and a length l_f and a diameter d_f are given to limit the fiber geometry, as illustrated in Figure 2.

All grids are traversed and located at a non-solid point. If the peripheral node redistribution of random number is, respectively, smaller than P , the point changes to solid phase.

Steps (2)–(4) are repeated until the solid-phase volume fraction reaches the previous setting value.

The procedure ended, and the results were output.

The microstructure of FPM is reconstructed according to six parameters: c_d , α and β , l_f , d_f , and ε . According to functions, α and β always constant values or random values. While l_f and d_f are defaulted to be random values in $[0, N_x]$ and $[2 \mu\text{m}, 4 \mu\text{m}]$, respectively. Furthermore, orientation angle θ_a is introduced and defined as the angle between fiber length direction and heat transfer direction. Two typical growth directions of fiber length are defined, which are perpendicular to heat transfer direction and parallel to heat transfer direction, and also a random number in uniform distribution $[0, 90^\circ]$. In Figure 2, we can see that the fibers interweave through each other rather than interpenetrate into each other. An interpenetrating rate is named to calculate the probability that one fiber interpenetrates another in random generating proceeding.

D3Q15LBM model, a 3D randomly constructed physical model of FPM, was applied to simulate the heat transfer process inside the material and predict its ETC. Due to the dense grid division, the generation and iterative evolution of physical models require a long time to complete, and the requirements for computer hardware are high. Mesh division that is too sparse may lead to significant differences between the constructed physical model and the actual microstructure, resulting in insufficient simulation accuracy. Considering the above two situations, the calculation domain is divided into $200 \times 200 \times 200$ with a grid step size of $\delta_X = 1 \mu\text{m}$. The FPM structure that was reconstructed by the modified model is shown in Figure 6.

2.2. ETC with LBM in Simulation

LBM is well suited to simulate heat transfer in resolving FPM. Two equations were combined to solve the conjugate heat transfer. One is involved in solving the diffusion equation, which was introduced in Section 2.2.1, and the other is relative to radiative transfer, which was described in Section 2.2.2.

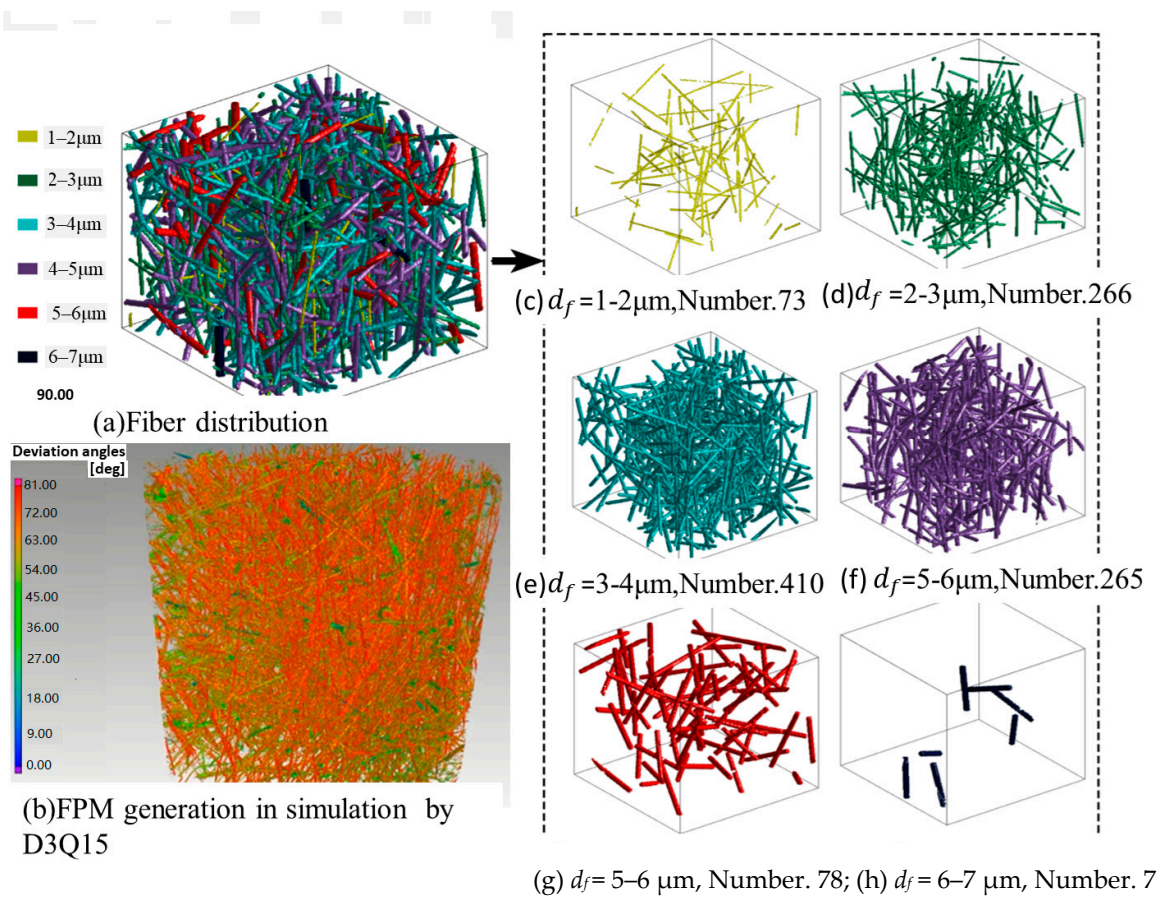


Figure 6. FPM generated with different parameters.

2.2.1. Energy Equations

The domain $\Omega = \Omega_f \cup \Omega_s$ is used to solve the energy equation, where Ω_f and Ω_s define the air and fiber domains (in Figure 7). Two diffusion equations for the T are solved by Wang's approach [23].

$$\rho_f c_{p,f} \frac{\partial T}{\partial t} = \lambda_f \nabla^2 T \text{ in } \Omega_f \quad (1)$$

$$\rho_s c_{p,s} \frac{\partial T}{\partial t} = \lambda_s \nabla^2 T \text{ in } \Omega_s \quad (2)$$

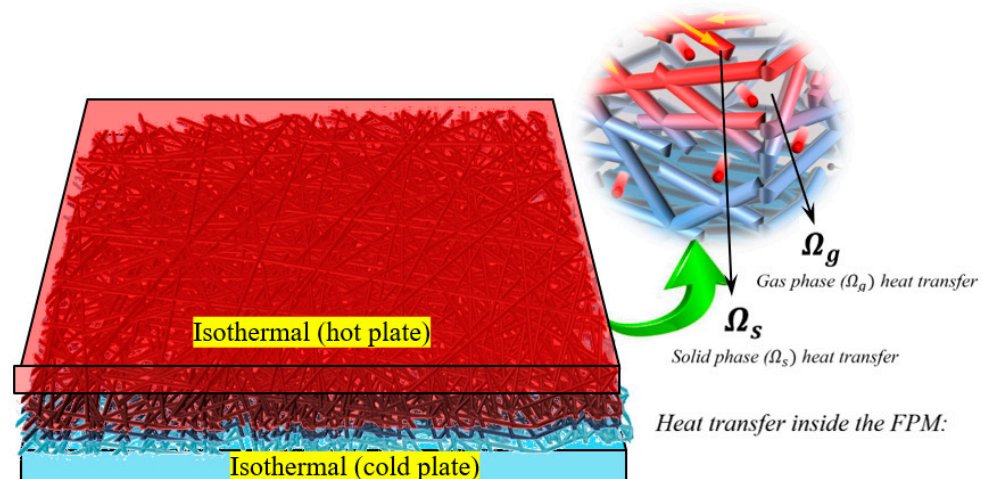


Figure 7. Schematic diagram of two domains.

The diffusion equation can be solved by:

$$f(x + \Delta x, t + \Delta t) = f_i - \frac{1}{\tau}(f_i - f_i^{eq}) \quad (3)$$

The equilibrium function f_i^{eq} is given according to [24].

$$f_i^{eq} = w_i T(x, t) \quad (4)$$

where $T(x, t)$ is local temperature and w_i is weight coefficient, calculated below [16]:

$$\omega_i = \begin{cases} 2/9 & i = 0 \\ 1/9 & i = 1 \sim 6 \\ 1/72 & i = 7 \sim 14 \end{cases} \quad (5)$$

The local temperature $T(x, t)$ and heat flux $q(x, t)$ are calculated by

$$T(x, t) = \sum_i f_i(x, t) \text{ and } q(x, t) = \frac{\tau - \frac{1}{2}}{\tau} \sum_{i=0}^6 c_i f_i(x, t) \quad (6)$$

Referring to Chapman–Enskog expansion [24],

$$\tau = \frac{\alpha}{c_s^2} + \frac{1}{2} \quad (7)$$

$$\alpha = \frac{\lambda}{\rho c_p} \text{ Additionally, } c_s = \frac{1}{\sqrt{4}} \cdot \tau |\Omega_s = \tau_s, \tau| \Omega_f = \tau_f \cdot \rho_{f*} = 1 \rho_{s*} = \rho_{f*} \frac{c_{p,f}}{c_{p,s}}$$

2.2.2. Radiation Equations

A. Mink et al. [36] introduced a mesoscopic sink term to solve the radiation transfer equation. Assumptions were proposed according to the P1-approximation-homogeneous participating media, spatially constant scattering, and absorption parameter σ_s and σ_a . Additionally, the radiation equation can then be modified as

$$\frac{1}{c} \frac{\partial \phi}{\partial t} = \frac{1}{3(\sigma_a + \sigma_s)} \nabla^2 \phi - \sigma_a \phi \quad (8)$$

where the artificial diffusion coefficient D is

$$D(\sigma_a, \sigma_s) = \frac{1}{3(\sigma_a + \sigma_s)} \quad (9)$$

$$g_i(x + \Delta x, t + \Delta t) = g_i - \frac{1}{\tau_g} (g_i - g_i^{eq}) - \frac{3\sigma_a(\sigma_a + \sigma_s)}{8} g_i \quad (10)$$

where $g_i^{eq} = w_i \phi$ and $\tau_g = 1$.

Based on distribution function's Zeroth moment, the spatial light intensity is

$$\phi(x) = \sum_i g_i \quad (11)$$

Following the Stephan–Boltzmann law, the boundary radiation intensities are chosen by

$$\phi = \left(\frac{T(x, t)}{T_{hot}} \right)^4 \quad (12)$$

2.2.3. ETC

Heat transfer in VIPs λ_g , λ_s , λ_r , and λ_c is summed.

$$\lambda_e = \lambda_g + \lambda_s + \lambda_r + \lambda_c \quad (13)$$

where λ_e in resolved packing is calculated by

$$\lambda_e = \frac{q_e L}{\Delta T} \quad (14)$$

where q_e is given by

$$q_e = q_s + q_f + q_r \quad (15)$$

q_r is calculated by

$$q_r = \sigma_a (4\sigma_b T^4 - \phi) \quad (16)$$

where, σ_b is the Stephan–Boltzmann constant.

The ECT is then gained in the simulation.

2.3. Variables in Simulation

λ_g (convection) is given by

$$\lambda_g = \frac{\lambda_{g0}}{(1 + 2\beta \cdot K_n)} \quad (17)$$

λ_{g0} is the effective thermal conductivity in continuum ($26.606 \times 10^{-3} \text{ W} \cdot \text{m}^{-1} \cdot \text{K}^{-1}$ [16]). β values for air and vapor are 1.63 and 1.5, respectively.

Along with inside air pressure decreasing, the heat transfer through the fluid decreases inversely proportional to Knudsen number [16].

$$K_n = \frac{l_f}{\Phi} \quad (18)$$

l_f can be given by

$$l_f = \frac{1}{\sqrt{2}\pi\sigma_g^2 n} \quad (19)$$

n is the number of molecules per volume $n = \frac{N}{V} [\text{m}^{-3}]$ and σ_g is the molecular diameter (air): $\sigma_g = (\sqrt{2}\pi l_f n)^{-1} = 3.7 \times 10^{-10} \text{ m}$.

The range of Knudsen number is $10^{-1} \leq K_n \leq 10^1$. Heat convection can be neglected when the pore size is smaller than 3 mm [16]. An initial δ is given in (20).

$$\delta = (2/3) \cdot d \cdot \pi / (1 - \pi) \quad (20)$$

ρ_f can be calculated by

$$\rho_f = \frac{p_g}{(R_s \cdot T)} \quad (21)$$

where R_s is $287.058 \text{ J} \cdot \text{kg}^{-1} \cdot \text{K}^{-1}$ [16] and T is 305.65 K .

σ_a is approximated as

$$\sigma_a = 9.2693 \times 10^{-3} \log(P) + 1.3437 \times 10^{-1} \log(P) + 4.7933 \times 10^{-1} \quad (22)$$

σ_s is given as 0.1 [16].

2.4. Thermal Boundary

The nonequilibrium distribution bounce-back rule is employed to solve isothermal boundary to calculate ETC; the boundary treatments in detail are illuminated in Table 1 and Figure 8.

Table 1. Boundary condition definition.

Items	Condition	Lbm Solution
Hot Plate	Isothermal boundary ($T_{hot} = 302$ K)	The nonequilibrium distribution Bounce-back rule
Cold Plate	Isothermal boundary ($T_{cold} = 298$ K)	The nonequilibrium distribution bounce-back rule
Top Wall	Adiabatic ($q = 0$)	Neumann boundary
Bottom Wall	Adiabatic ($q = 0$)	Neumann boundary
Front Wall	Adiabatic ($q = 0$)	Neumann boundary
Back Wall	Adiabatic ($q = 0$)	Neumann boundary

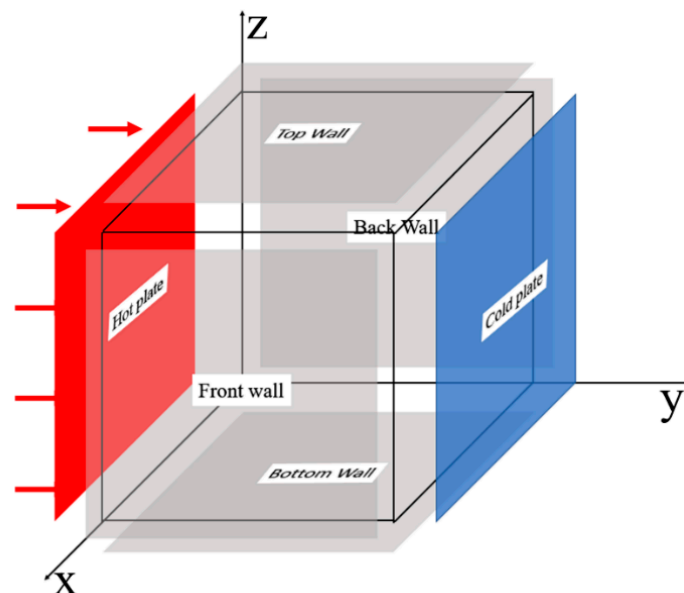


Figure 8. Schematic diagram of boundary.

2.5. Measurement Device

To collect the ETC of VIPs, the experimental devices were set up. The inter-pressure in VIPs is the key parameter to evaluate the thermal insulation properties. A vacuum apparatus including a pressure sensor, valve, on/off, and pressure gauge was designed to measure the final vacuum degree. The schematic is shown in Figure 9a. The typical accuracy of the measurement is $\pm 3\%$.

To measure ETC of samples (in Figure 9b) versus various internal pressures, the guarded hot plate apparatus is employed. The measurement system is shown in Figure 9c,d.

In this system, a heating block is located in center. An electric heating unit is installed in heating block. It is made of pure copper with the size $150 \times 150 \times 50$ mm³. The heating block is surrounded by a guard plate. The specimen is placed between cold plate and heating block/guard plate. Both cold and hot plates are made of pure copper, and the sizes of both are $300 \times 300 \times 50$ mm³. The temperatures of both plates are maintained constant by an isothermal water tank.

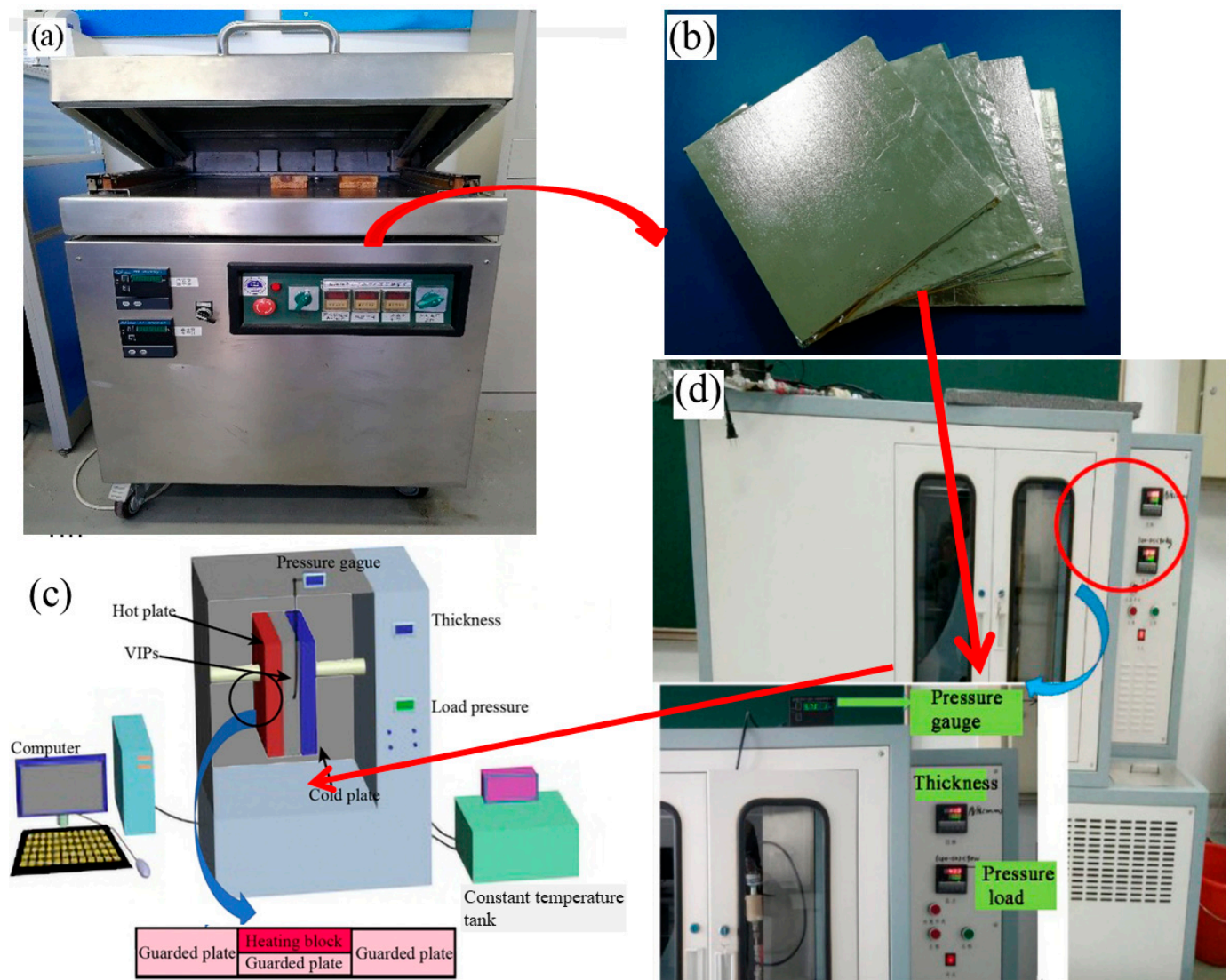


Figure 9. Experimental devices involved in this work: (a) vacuum packing apparatus; (b) VIP specimens for experiments; (c) Schematic diagram of ETC measurement apparatus; (d) measurement apparatus of ETC.

In measuring the ETC of specimen, the cold plate is held at a constant temperature of 15 °C while the hot plate maintains a constant 35 °C. The power required to maintain the hot plate temperature is recorded. The ETC is automatically reported once the temperature reaches stable value.

3. Results and Discussion

In this section, the LBM is performed to investigate the effects of gas pressure, fiber diameter, and orientation angle on the ETC of the FPM, especially on the ETC. All the unspecified values are set as default.

3.1. ETC Versus Gas Pressure and Fiber Diameter

Gas pressure seriously affected heat transfer through VIPs with the FPM core. The mentioned literature above reflected that the FPM can gain an excellent adiabatic performance in extremely low pressure (≤ 50 Pa). However, it is sensitive to pressure fluctuation [18,36]. The reason may be due to its high open cell rate and large pore size against other materials. The above literature did not directly explore the effects of fiber diameter. In this work, five diameters, that is, $d_f = 1 \mu\text{m}$, $2 \mu\text{m}$, $4 \mu\text{m}$, $6 \mu\text{m}$, and $7 \mu\text{m}$ are involved,

and the microstructure was reconstructed with $\varepsilon = 0.9$, $c_d = 0.0001$; $l_f = U(0, N_x)$; and $\theta_a = U(0, \pi)$. λ_e versus d_f illuminates the similar trend as P_g changes, which is shown in Figure 10. With $\lambda_e = 8 \text{ mW} \cdot \text{m}^{-1} \cdot \text{K}^{-1}$ as the failure threshold, $d_f = 7 \text{ } \mu\text{m}$ obtained the threshold value, while the P_g was 100 Pa. The finer the fiber diameter is, the higher the failure pressure is. The Knudsen can be introduced to illuminate. The characteristic pore size (l_{cs}) is close to diameter. The fiber diameter of the microstructure in Figure 3a was finer than that in Figure 3b. A finer fiber diameter means more fibers were required to gain the same porosity. The smaller pore size and more uniform pore distribution exhibited in Figure 3a are better than that in Figure 3b.

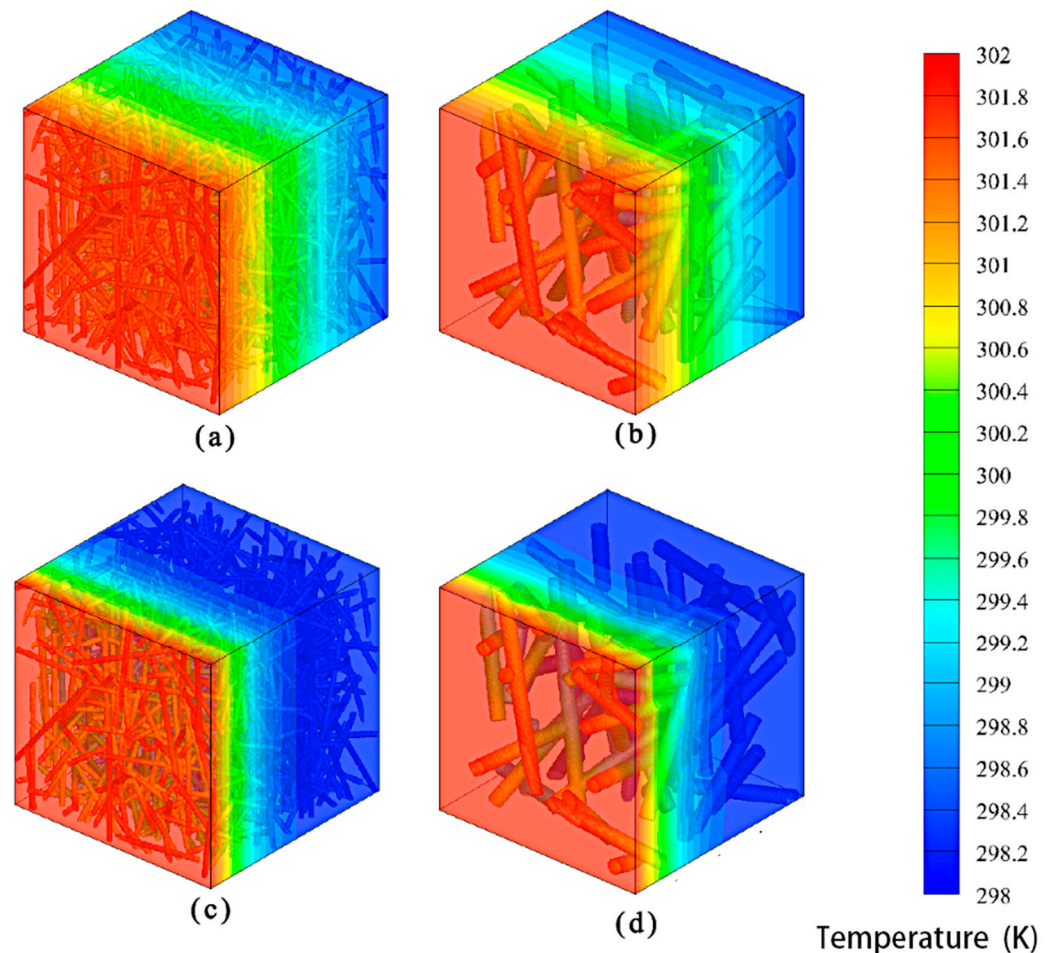


Figure 10. Temperature distribution in simulation ($\varepsilon = 0.9$, $c_d = 0.001$, $l_f = \text{default}$, and $\theta_a = \text{default}$) under two pressures at the steady condition: (a) $d_f = 1 \text{ } \mu\text{m}$; $P_g = 10^5 \text{ Pa}$; (b) $d_f = 7 \text{ } \mu\text{m}$; $P_g = 10^5 \text{ Pa}$; (c) $d_f = 1 \text{ } \mu\text{m}$; $P_g = 1 \text{ Pa}$; and (d) $d_f = 7 \text{ } \mu\text{m}$; $P_g = 1 \text{ Pa}$.

The average diameter of FPM is a controllable parameter in simulation. It is necessary to understand the effects of this parameter on ETC. Here, the mean diameter of FPM varied from $1 \text{ } \mu\text{m}$ to $8 \text{ } \mu\text{m}$ to disclose the mean diameter impacting the ETC. The results shown in Figure 11 indicated that the ETC of the small mean diameter was much lower than that of the larger mean diameter, especially when the gas pressure exceeded 10 Pa. The reason for this behavior is that the suppression of gaseous ETC is due to the reduced smaller pore size. It is visible in the shape of the fitting data, where the second inflection point in the “S-shape” curve presents at gas pressures above 100 Pa. In addition, with the decrease in the mean diameter of glass fiber, the porosity became lower and lower, and the lower critical pressure decreased. From the results shown in Figure 10, it is suggested that the mean diameter of ultrafine glass fibers should be preferred at $1 \text{ } \mu\text{m}$ to obtain the lower thermal conductivity; however, the cost would increase significantly from the perspective of pro-

ducers. Hence, the mean diameter of ultrafine glass fibers would be a flexible option, and a reasonable mean diameter and economy should be considered for various applications.

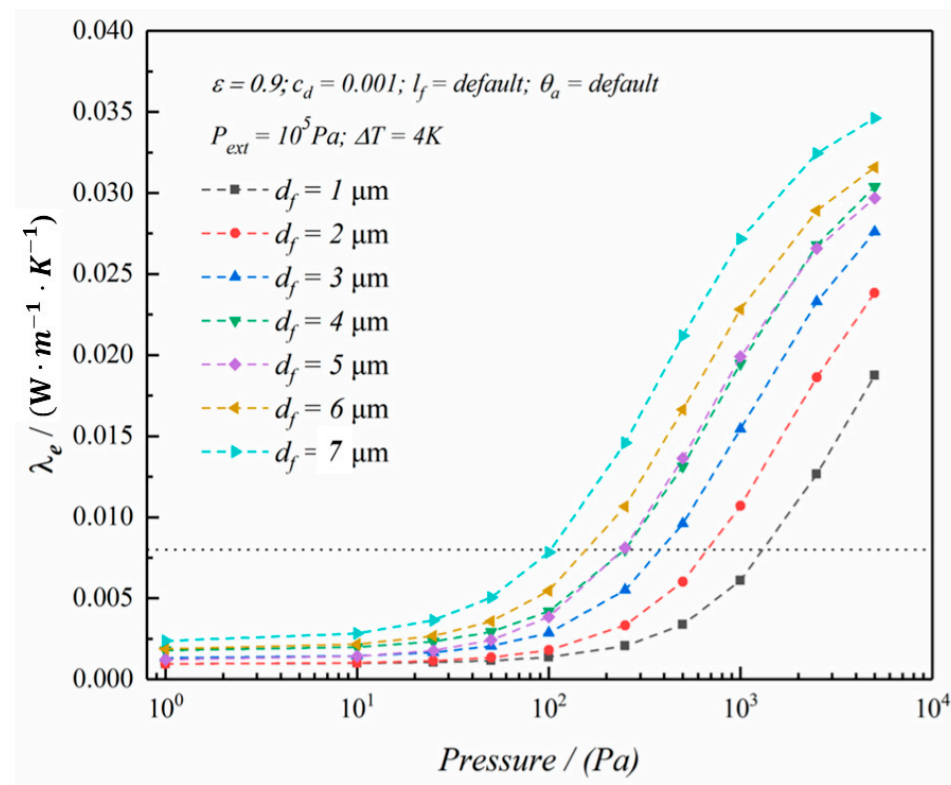


Figure 11. Pressure dependence of the λ_e versus d_f .

Five specimens of VIPs were fabricated under the same conditions, but at different pressures varying from 0.1 Pa to 100 Pa. The comparison between experimental and predictive ETC is shown in Table 2. λ_e curves varying with vacuum are shown in Figure 11.

Table 2. The comparison of experimental and predictive ETCs.

Items	Specimen				
	1	2	3	4	5
Initial air pressure/Pa	0.1	1	10	100	1000
Measured ETC/ $\text{W}\cdot\text{m}^{-1}\cdot\text{K}^{-1}$	2.68	2.96	3.19	5.84	14.63
Predictive ETC/ $\text{W}\cdot\text{m}^{-1}\cdot\text{K}^{-1}$	2.61	2.83	2.94	4.86	10.44
error	0.03	0.04	0.08	0.17	0.29

The ETC of VIPs was measured by the formerly mentioned apparatus. Each specimen was measured five times to reduce the error. Additionally, the average value was adopted as the final experimental value. The predictive values can be calculated by the developed model, and the error between experimental and theoretical values can be obtained.

The deviation between experimental and predictive ETC was due to the gases outgassing from the FPM and permeating into the panel through the barrier. It indicated that when the pressure was less than 10 Pa, the ETCs of both values were close, and both of them were no more than $4.0 \text{ m}\cdot\text{W}\cdot\text{m}^{-1}\cdot\text{K}^{-1}$. While the inside pressure exceeded 10 Pa, the measured ETC increased sharply. With the pressure increasing, the deviation increased between measured and calculated values. The reason for this is that high pressure resulted in thermal convection, and the coupling thermal conductivity was ignored in the predictive model. Once the free path of the air molecules in the pores is smaller than that of

the pore size, the convective heat transfer will be notable, and the ETC of the VIPs will increase sharply.

3.2. The Effect of Orientation Angle on ETC

Two growth directions of fiber were involved in this work: perpendicular or/and parallel to the heat transfer direction. λ_e curves varying with the angle in vacuum 10 Pa are shown in Figure 12. An increase in orientation angle resulted in a subsequent λ_e , which dropped until the angle was at 90°; meanwhile, λ_e reached the minimum value. Further conclusions can be gained in Figure 13: that the heat transfer of fiber directionally increased, and the heat transfer was biased toward the fiber length direction. When the orientation angle was 90°, the heat path mainly went along with the interface perpendicular to the direction (in Figure 13a). When the orientation angle decreased, the heat path shortened, and the temperature field could be noticeably degraded (shown in Figure 13b–d). In addition, the λ_e variation range expanded under low pressure. The reason was that gas heat conduction was greatly suppressed in a vacuum, and the proportion of fiber heat conduction in ETC increased.

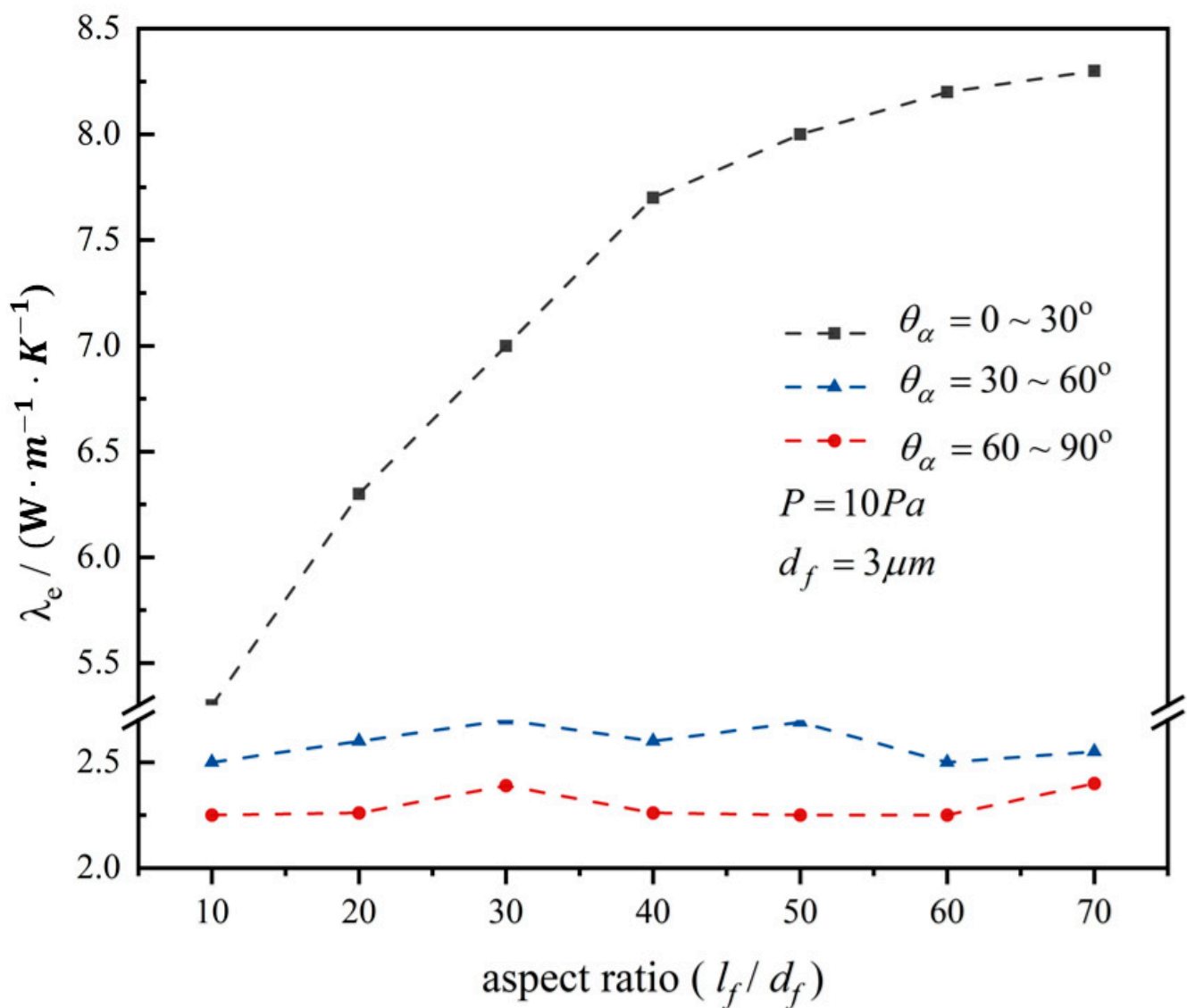


Figure 12. Trend of ETC versus orientation angles.

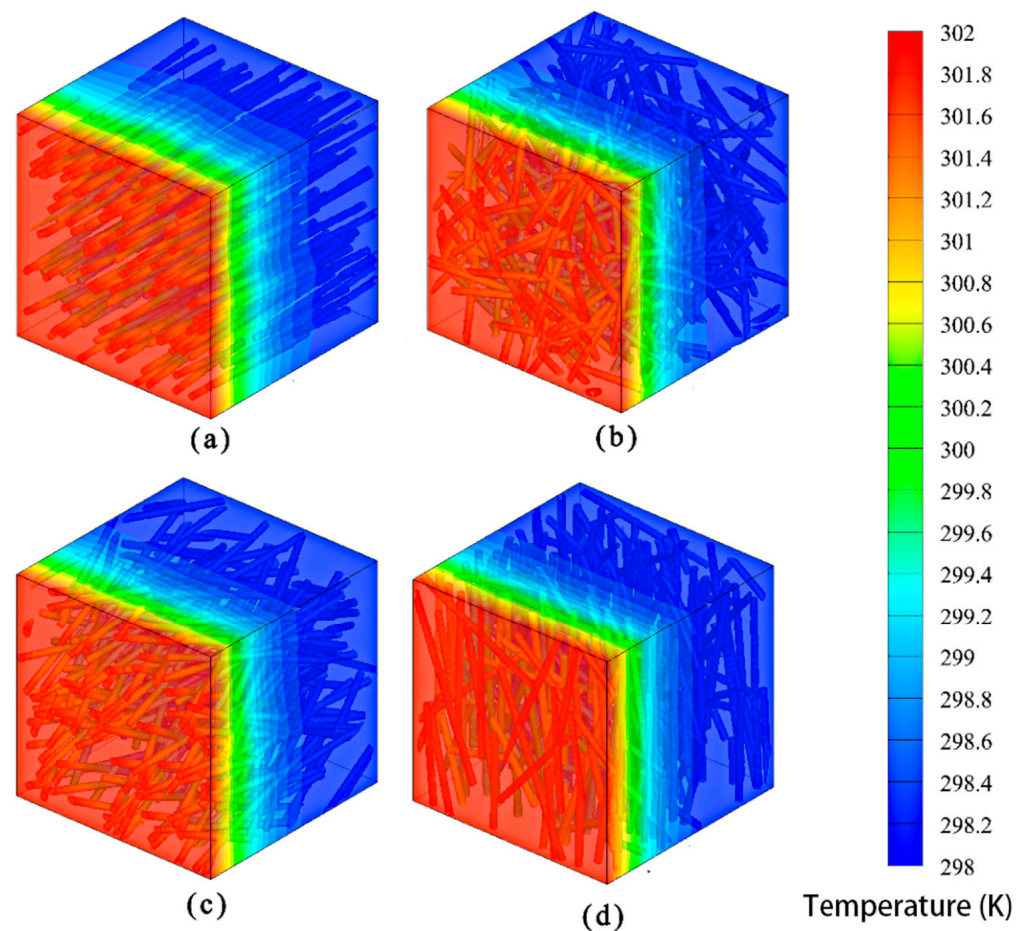


Figure 13. Temperature distributions in Simulation ($\varepsilon = 0.9$, $c_d = 0.001$, $l_f = \text{default}$, $d_f = 4 \mu\text{m}$, and $P_g = 10 \text{ Pa}$) with different orientation angles at the steady state: (a) $\theta_a = 0^\circ$; (b) $\theta_a = 30^\circ$; (c) $\theta_a = 60^\circ$; and (d) $\theta_a = 90^\circ$.

4. Conclusions

A modified D3Q15-LBM was proposed in this work to investigate the dependencies of ETC on FPM microstructure in a vacuum. The model is theoretically and experimentally validated. The parameters involved were concentrated to illuminate the significant impacts on FPM. Conclusions can be made into the following points:

- (1) The influences of five microstructure parameters, that is, the generation probability of nucleus growth, fiber length, diameter, coincidence rate, and orientation angle on ETC, are highlighted;
- (2) Based on five structural parameters, an improved generation approach, D3Q15-LBM, was deduced. The model is validated with influences of different microstructure parameters;
- (3) The effects of microstructure parameters were numerically analyzed, and the model was validated. It indicated that an FPM structure with a finer diameter and smaller pore size had a more excellent ability to maintain a lower ETC in a higher vacuum. The ETC was also affected by the orientation angles of fibers. The more the heat transfer direction is inconsistent with the length direction of the fiber, the better the adiabatic performance is;
- (4) The reliability of the model is verified by comparison with the experimental values. Additionally, a suggestion was made that low ETC of VIPs by optimizing the microstructure of FPM and increasing the vacuum can be obtained. The work is a reference to optimize the FPM core of VIPs.

Author Contributions: Conceptualization, B.C. and A.K.; methodology, A.K.; software, J.Z.; validation, L.Y., J.Z. and B.C.; formal analysis, B.C.; investigation, B.C.; resources, A.K.; data curation, J.Z.; writing—original draft preparation, B.C.; writing—review and editing, A.K. and L.Y.; visualization, Z.C.; supervision, Z.C.; project administration, A.K.; funding acquisition, Z.C. All authors have read and agreed to the published version of the manuscript.

Funding: The work was supported by the joint fund of the National Natural Sciences Foundation of China (grant number: U2167214), in part by the Shanghai Frontiers Science Center of “Full Penetration” Far-Reaching Offshore Ocean Energy and Power.

Data Availability Statement: The datasets supporting the conclusions of this article are included within the article and the sequencing data correspond with Figs. It will be made available upon reasonable academic request within the limitations of informed consent by the corresponding author upon acceptance.

Acknowledgments: The authors would also like to render thanks to Shanghai Polytechnic University for the SEM and scientist Samuel Brunner for his assistance in the experimental method. The author thanks Dan Cao and Wei Wang, Shanghai Maritime University, for their kind suggestions.

Conflicts of Interest: The authors declare that they have no known competing financial interest or personal relationships that could have appeared to influence the work reported in this paper.

Nomenclature

ETC/λ_e	effective thermal conductivity, $W \cdot m^{-1} \cdot K^{-1}$
FPM	fibrous porous medium
λ	thermal conductivity, $W \cdot m^{-1} \cdot K^{-1}$
N_x	lattice number of corresponding dimension
x_0	core growth coordinate
c_d	core distribution probability
α	angle between z-axis and fiber, $^\circ$
β	angle of fiber with y-axis in Z plane, $^\circ$
l_f	fiber length, μm
l_{cs}	characteristic size of cells, m
$d_{(x,y,z)}$	normal distance, μm
$l_{(x,y,z)}$	axial distance, μm
θ_a	orientation angle, $^\circ$
λ_s	solid thermal conductivity, $W \cdot m^{-1} \cdot K^{-1}$
λ_g	gas thermal conductivity, $W \cdot m^{-1} \cdot K^{-1}$
λ_c	convection thermal conductivity, $W \cdot m^{-1} \cdot K^{-1}$
λ_r	radiation thermal conductivity, $W \cdot m^{-1} \cdot K^{-1}$
λ_{coup}	coupling thermal conductivity, $W \cdot m^{-1} \cdot K^{-1}$
λ_{leak}	leakage thermal conductivity, $W \cdot m^{-1} \cdot K^{-1}$
λ_{g0}	free space gas thermal conductivity, $W \cdot m^{-1} \cdot K^{-1}$
ρ	density, $kg \cdot m^{-3}$
d_g	diameter of the air molecules, $3.72 \times 10^{-10} m$
ε	porosity
d_f	fiber diameter, μm
T	temperature, K
P_g	gas pressure, Pa
i	discrete direction
x	location vector
e_i	discrete velocity
t	discrete time
f_i^{eq}	local equilibrium function
w_i	weight coefficient
$T(x, t)$	local temperature, K
τ	dimensional relaxation time
c	lattice sound speed

β_e	energy transfer efficiency
K_n	Knudsen number
K_B	Boltzmann constant, 1.38×10^{-23} J·K
f_i	temperature evolution function
L	plate distance, m
ΔT	temperature difference, K
q	heat flux, $W \cdot m^{-2}$
c_p	specific heat capacity, $J \cdot kg^{-1} \cdot K^{-1}$
P_{ext}	external pressure, Pa
δt	time step, usually given as 1

References

- Fang, K.; Li, C.; Tang, Y.; He, J.; Song, J. China's pathways to peak carbon emissions: New insights from various industrial sectors. *Appl. Energy* **2021**, *306*, 118039. [\[CrossRef\]](#)
- NDRC. *The People's Republic of China Second Biennial Update Report on Climate Change*; China Planning Press: Beijing, China, 2018. Available online: <https://english.mee.gov.cn/Resources/Reports/reports/201907/P020190702568751604320.pdf> (accessed on 30 December 2018).
- Fang, K.; Zhang, Q.; Long, Y.; Yoshida, Y.; Sun, L.; Zhang, H.; Dou, Y.; Li, S. How can China achieve its Intended Nationally Determined Contributions by 2030? A multi-criteria allocation of China's carbon emission allowance. *Appl. Energy* **2019**, *241*, 380–389. [\[CrossRef\]](#)
- Mallapaty, S. How China could be carbon neutral by mid-century. *Nature* **2020**, *586*, 482–483. [\[CrossRef\]](#)
- Mora, C.; Rollins, R.L.; Taladay, K.; Kantar, M.; Chock, M.K.; Shimada, M.; Franklin, E.C. Bitcoin emissions alone could push global warming above 2 °C. *Nat. Clim. Chang.* **2018**, *8*, 931–933. [\[CrossRef\]](#)
- McGlade, C.; Ekins, P. The geographical distribution of fossil fuels unused when limiting global warming to 2 °C. *Nature* **2015**, *517*, 187–190. [\[CrossRef\]](#)
- The State Council of China. Report on the Work of the Government. 2020. Available online: http://english.www.gov.cn/premier/news/202005/30/content_WS5ed197f3c6d0b3f0e94990da.html (accessed on 30 May 2020).
- Jiang, J.; Ye, B.; Liu, J. Peak of CO₂ emissions in various sectors and provinces of China: Recent progress and avenues for further research. *Renew. Sustain. Energy Rev.* **2019**, *112*, 813–833. [\[CrossRef\]](#)
- Liu, Z.; Guan, D.; Wei, W.; Davis, S.J.; Ciais, P.; Bai, J.; Peng, S.; Zhang, Q.; Hubacek, K.; Marland, G.; et al. Reduced carbon emission estimates from fossil fuel combustion and cement production in China. *Nature* **2015**, *524*, 335–338. [\[CrossRef\]](#) [\[PubMed\]](#)
- Song, J.; Yang, W.; Wang, S.; Wang, X.; Higano, Y.; Fang, K. Exploring potential pathways towards fossil energy-related GHG emission peak prior to 2030 for China: An integrated input-output simulation model. *J. Clean. Prod.* **2018**, *178*, 688–702. [\[CrossRef\]](#)
- Gallagher, K.S.; Zhang, F.; Orvis, R.; Rissman, J.; Liu, Q. Assessing the Policy gaps for achieving China's climate targets in the Paris Agreement. *Nat. Commun.* **2019**, *10*, 1256. [\[CrossRef\]](#) [\[PubMed\]](#)
- Viebahn, P.; Vallentin, D.; Höller, S. Prospects of carbon capture and storage (CCS) in China's power sector—An integrated assessment. *Appl. Energy* **2015**, *157*, 229–244. [\[CrossRef\]](#)
- Pan, X.; Wang, H.; Wang, L.; Chen, W. Decarbonization of China's transportation sector: In light of national mitigation toward the Paris Agreement goals. *Energy* **2018**, *155*, 853–864. [\[CrossRef\]](#)
- Kan, A.; Zheng, N.; Zhu, W.; Cao, D.; Wang, W. Innovation and development of vacuum insulation panels in China: A state-of-the-art review. *J. Build. Eng.* **2022**, *48*, 103937. [\[CrossRef\]](#)
- Chen, X.; Shuai, C.; Wu, Y.; Zhang, Y. Analysis on the carbon emission peaks of China's industrial, building, transport, and agricultural sectors. *Sci. Total. Environ.* **2019**, *709*, 135768. [\[CrossRef\]](#) [\[PubMed\]](#)
- Lu, J.; Kan, A.; Zhu, W.; Yuan, Y. Numerical investigation on effective thermal conductivity of fibrous porous medium under vacuum using Lattice-Boltzmann method. *Int. J. Therm. Sci.* **2020**, *160*, 106682. [\[CrossRef\]](#)
- Simmler, H.; Brunner, S. Vacuum insulation panels for building application: Basic properties, aging mechanisms and service life. *Energy Build.* **2005**, *37*, 1122–1131. [\[CrossRef\]](#)
- Mao, S.; Kan, A.; Zhu, W.; Yuan, Y. The impact of vacuum degree and barrier envelope on thermal property and service life of vacuum insulation panels. *Energy Build.* **2019**, *209*, 109699. [\[CrossRef\]](#)
- Alam, M.; Singh, H.; Limbachiya, M. Vacuum Insulation Panels (VIPs) for building construction industry—A review of the contemporary developments and future directions. *Appl. Energy* **2011**, *88*, 3592–3602. [\[CrossRef\]](#)
- Kan, A.; Mao, S.; Wang, N.; Shi, B. Simulation and Experimental Study on Thermal Conductivity of Nano-Granule Porous Material Based on Lattice-Boltzmann Method. *J. Therm. Sci.* **2019**, *30*, 248–256. [\[CrossRef\]](#)
- Wang, M.; Wang, X.; Wang, J.; Pan, N. Grain size effects on effective thermal conductivity of porous materials with internal thermal contact resistance. *J. Porous Media* **2013**, *16*, 1043–1048. [\[CrossRef\]](#)
- Tugnoli, A.; Moricone, R.; Scarponi, G.E.; Cozzani, V. Effective thermal conductivity of fibrous fireproofing materials. *Int. J. Therm. Sci.* **2018**, *136*, 107–120. [\[CrossRef\]](#)

23. Xiao, T.; Guo, J.; Yang, X.; Hooman, K.; Lu, T.J. On the modelling of heat and fluid transport in fibrous porous media: Analytical fractal models for permeability and thermal conductivity. *Int. J. Therm. Sci.* **2021**, *172 Pt A*, 107270. [[CrossRef](#)]
24. Wang, M.; Wang, J.; Pan, N.; Chen, S. Mesoscopic predictions of the effective thermal conductivity for microscale random porous media. *Phys. Rev. E* **2007**, *75*, 036702. [[CrossRef](#)]
25. Mendes, M.A.; Ray, S.; Trimis, D. A simple and efficient method for the evaluation of effective thermal conductivity of open-cell foam-like structures. *Int. J. Heat Mass Transf.* **2013**, *66*, 412–422. [[CrossRef](#)]
26. Lin, Y.; Yang, C.; Zhang, W.; Fukumoto, K.; Saito, Y.; Machida, H.; Norinaga, K. Estimation of effective thermal conductivity in open-cell foam with hierarchical pore structure using lattice Boltzmann method. *Appl. Therm. Eng.* **2022**, *218*, 119314. [[CrossRef](#)]
27. Wei, G.; Liu, Y.; Zhang, X.; Yu, F.; Du, X. Thermal conductivities study on silica aerogel and its composite insulation materials. *Int. J. Heat Mass Transf.* **2011**, *54*, 2355–2366. [[CrossRef](#)]
28. Bi, C.; Tang, G.H.; Hu, Z.J.; Yang, H.L.; Li, J.N. Coupling model for heat transfer between solid and gas phases in aerogel and experimental investigation. *Int. J. Heat Mass Transf.* **2014**, *79*, 126–136. [[CrossRef](#)]
29. Farahani, M.V.; Hassanpouryouzband, A.; Yang, J.; Tohidi, B. Heat Transfer in Unfrozen and Frozen Porous Media: Experimental Measurement and Pore-Scale Modeling. *Water Resour. Res.* **2020**, *56*, e2020WR027885. [[CrossRef](#)]
30. Qu, Z.G.; Fu, Y.D.; Liu, Y.; Zhou, L. Approach for predicting effective thermal conductivity of aerogel materials through a modified lattice Boltzmann method. *Appl. Therm. Eng.* **2018**, *132*, 730–739. [[CrossRef](#)]
31. Ross-Jones, J.; Gaedtke, M.; Sonnick, S.; Rädle, M.; Nirschl, H.; Krause, M.J. Conjugate heat transfer through nano scale porous media to optimize vacuum insulation panels with lattice Boltzmann methods. *Comput. Math. Appl.* **2018**, *77*, 209–221. [[CrossRef](#)]
32. Guo, C.; Nian, X.; Liu, Y.; Qi, C.; Song, J.; Yu, W. Analysis of 2D flow and heat transfer modeling in fracture of porous media. *J. Therm. Sci.* **2017**, *26*, 331–338. [[CrossRef](#)]
33. Gaedtke, M.; Wachter, S.; Kunkel, S.; Sonnick, S.; Rädle, M.; Nirschl, H.; Krause, M.J. Numerical study on the application of vacuum insulation panels and a latent heat storage for refrigerated vehicles with a large Eddy lattice Boltzmann method. *Heat Mass Transf.* **2019**, *56*, 1189–1201. [[CrossRef](#)]
34. Wu, Y.; Shi, Y.; Cai, N.; Ni, M. Thermal Modeling and Management of Solid Oxide Fuel Cells Operating with Internally Reformed Methane. *J. Therm. Sci.* **2018**, *27*, 203–212. [[CrossRef](#)]
35. Liu, J.; Liu, S.; Sun, S.; Zhou, W.; Schlager, I.H.I.; Wang, M.; Yan, Y. Tomographic data fusion with CFD simulations associated with a planar sensor. *J. Therm. Sci.* **2017**, *26*, 175–182. [[CrossRef](#)]
36. Mink, A.; Thäter, G.; Nirschl, H.; Krause, M.J. A 3D Lattice Boltzmann method for light simulation in participating media. *J. Comput. Sci.* **2016**, *17*, 431–437. [[CrossRef](#)]

Disclaimer/Publisher’s Note: The statements, opinions and data contained in all publications are solely those of the individual author(s) and contributor(s) and not of MDPI and/or the editor(s). MDPI and/or the editor(s) disclaim responsibility for any injury to people or property resulting from any ideas, methods, instructions or products referred to in the content.